Topographic effects on wave resonance in the narrow gap between fixed box and vertical wall

Junliang Gao[1, 2], Zhiwei He[1], Jun Zang[2 *], Qiang Chen[2], Haoyu Ding[2], Gang Wang[3]

1. School of Naval Architecture and Ocean Engineering, Jiangsu University of Science and Technology, Zhenjiang 212003, China

2. Research Unit for Water, Environment and Infrastructure Resilience (WEIR), Department of Architecture and Civil Engineering, University of Bath, BA2 7AY, U.K.

3. College of Harbour, Coastal and Offshore Engineering, Hohai University, Nanjing 210098, China

Abstract:

Multiple coastal and offshore structures deployed side by side with narrow gap may be subject to large-amplitude free surface resonance, which can lead to green water on the deck and cause rapid increase of hydrodynamic loading on structures. Here, the resonant motions of the free surface inside a narrow gap between a fixed box and a vertical wall excited by incident regular waves with various wave heights are simulated using a two-dimensional numerical wave tank. The topographies of plane slopes with different inclinations are deployed in front of the vertical wall. The main focus of this paper is on the influences of the topographical variation on the fluid resonance inside the narrow gap. For the first time, it is found that the fluid resonant frequency decreases monotonously with the topographical slope, and both the amplification of the resonant wave height and the reflection coefficient present a pattern of fluctuation with the slope. For all the topographies considered in this paper, both the fluid resonant frequency and the amplification of the resonant wave height are shown to decrease with the incident wave height; while the variation trend of the reflection coefficient with the incident wave height depends on the topographical slope.

Keywords: Gap resonance; Topographical effects; Resonant frequencies; Resonant wave height; Reflection coefficient; OpenFOAM®

1. Introduction

* Corresponding author. E-mail: J.Zang@bath.ac.uk.

Multiple marine structures deployed side by side with small separation distances are commonly adopted in the field of coastal and offshore engineering. For example, large scale bottom-mounted rectangular caissons with small gaps in between are widely used in real harbors (Miao et al., 2001; Zhu et al., 2017). Liquefied natural gas (LNG) shuttle carriers and Floating Production Storage and Offloading (FSPO) units are often arranged side by side with narrow gaps between them as the LNG production is carried from the FSPO platform to the LNG shuttle carrier (Zhao et al., 2018a; Zhao et al., 2018b). Large-amplitude free surface resonance may be excited in the narrow gap under certain wave conditions, and this phenomenon is normally referred to as "gap resonance". Gap resonance can lead to the green water on the deck and cause the rapid increase of hydrodynamic forces on structures compared with the hydrodynamic forces on the same structure in isolation, which would seriously threaten the safety of engineering operations. Hence, in order to achieve the increased safety of the engineering operations related to the gap resonance phenomenon, more efforts should be made to improve the understanding of the mechanisms of hydrodynamics.

The methods utilized in the investigation of the gap resonance problem include theoretical analyses, laboratory experiments, and numerical simulations. The theoretical analyses were mainly adopted in the early-stage study of gap resonance and were mainly based on the linear potential flow theory. By combining the linear potential flow theory with an asymptotic matching technique, Miao et al. (2000; 2001) analytically investigated the gap effects on multiple floating bodies and on twin bottom-mounted rectangular caissons, respectively. Similarly, based on the linear potential flow theory and through solving an eigenvalue equation, Molin (2001) obtained a theoretical solution for the resonant frequencies of piston- and sloshing-modes for the barges with infinite length and breadth in the infinite water depth. Subsequently, Molin et al. (2002) further extended this work to the gap resonance in an open-ended narrow gap. To understand gap resonance better and to examine previous theoretical analyses, many laboratory experiments were further carried out. Saitoh et al. (2006) and Iwata et al. (2007) implemented a series of two-dimensional physical model experiments in a wave tank to investigate the fluid resonance inside a narrow gap formed by two fixed boxes and that inside two narrow gaps formed by three fixed boxes, respectively. Similarly, Tan et al. (2014) conducted two-dimensional physical experiments to consider the fluid resonance and energy dissipation in a narrow gap formed by a fixed rectangular box in front of a vertical wall. To study the free-surface resonance between the FSPO terminal and the LNG shuttle carrier or between two

barges, some three-dimensional physical tests were successively carried out by Clauss et al. (2013), Xu et al. (2014), Li et al. (2016) and Zhao et al. (2017).

The numerical studies implemented so far mainly employed the classical potential flow model combining with the boundary element method or scaled boundary finite element method (e.g., Miao et al. (2001), Li et al. (2005), Zhu et al. (2008), Sun et al. (2010) and Li and Zhang (2016)). Because the energy dissipation caused by the fluid viscosity, vortex shedding and even turbulence cannot be considered in the context of the potential flow theory, although both the theoretical analyses and the numerical simulations that are based on the potential flow model have been proved to predict the resonant frequency well, they were reported to overestimate the resonant wave height in the gap and the wave forces on the structures significantly. In order to overcome this deficiency, so far, several particular numerical techniques have been proposed to artificially produce and introduce the energy dissipation into the potential flow model (Chen, 2004; Huijsmans et al., 2001; Newman, 2004; Ning et al., 2015a, b). The comparisons between numerical and experimental results demonstrate that the potential flow model with the artificial energy dissipative term may estimate the resonant wave height and the corresponding wave forces satisfactorily (Lu et al., 2011a; Lu et al., 2011b). Nevertheless, for the rigorous potential theory, the introduction of artificial energy dissipative term seems somewhat arbitrary, and under certain circumstances it was found to be difficult to achieve a unique value for the dissipative parameter (Liu and Li, 2014; Pauw et al., 2007; Tan et al., 2014). Therefore, careful calibrations are indispensable by using Computational Fluid Dynamics (CFD) results or available experimental data.

Due to the rapid developments of computing technology and numerical technique, the CFD based numerical simulations have gradually become an effective alternative method in studying the gap resonance problem in recent years. By using a Navier-Stokes equations model combined with a CLEAR-VOF technique for free surface capture, Lu et al. (2011a) and Lu et al. (2011b) systematically investigated the resonant wave height inside the narrow gap between multi-bodies in close proximity and the corresponding wave forces on the multi-bodies, respectively. Subsequently, based on an open-source CFD package OpenFOAM®, Moradi et al. (2015) and Moradi et al. (2016) comprehensively studied the influences of inlet configuration and water depth on wave resonance in the narrow gap between two fixed bodies, respectively. Recently, Feng et al. (2017) adopted OpenFOAM® to examine the viscous effects on the gap resonance between two side-by-side barges.

More recently, also based on the OpenFOAM® model, Jiang et al. (2018) and Jiang et al. (2019) investigated the wave resonance between two side-by-side non-identical boxes and the corresponding wave forces on both boxes by utilizing a two-dimensional numerical wave tank. Subsequently, Gao et al. (2019a) also employed OpenFOAM® to systematically investigate various hydrodynamic characteristics of the gap resonance between two fixed boxes in close proximity, which include the harmonic analyses of the free-surface elevation inside the gap and wave loads on both boxes, the effects of the incident wave height on the reflection, transmission and energy loss coefficients, and the quantitative estimation of the response time and the damping time of gap resonance. All these investigations found that the numerical results obtained by the CFD simulations agreed very well with the available experimental data.

Although numerous research efforts into the gap resonance problem have been performed, the majority have concentrated on the analyses of the wave resonance in the gap formed by the multiple floating (or fixed) structures and the corresponding wave loads on these structures (e.g., Feng and Bai (2015); Feng et al. (2017); Jiang et al. (2019); Jiang et al. (2018); Lu et al. (2011a); Lu et al. (2011b); Moradi et al. (2015, 2016); Ning et al. (2016); Ning et al. (2018); Zhu et al. (2017)). The investigations on the fluid resonance inside the narrow gap formed by a large vessel berthing in front of a wharf are relatively rare. By combining the numerical simulations and physical model experiments, Kristiansen and Faltinsen (2009) investigated the resonant behavior of the fluid in the gap between a ship and a fixed bottom-mounted terminal subject to incoming waves in shallow water, and the ship was restrained from moving. By employing both laboratory experiments and a semi-analytical analysis, Tan et al. (2014) investigate the mechanical energy dissipation involved in the fluid resonance inside a narrow gap between a fixed floating box and a vertical wall. Recently, Meringolo et al. (2018) adopted a two-dimensional Smoothed Particles Hydrodynamics (SPH) model to perform an energy balance analysis for the fluid resonance problem occurred in the gap formed by a fixed barge placed in front of a vertical wall. It should be noted that in all of these three papers, the seabed in front of the bottom-mounted terminal (or the vertical wall) was always assumed to be flat, and the effects of the topographical variation on gap resonance were not taken into consideration. In fact, the bottom inside real harbors is usually uneven and the water depth in front of the terminal is often variable on most occasions (Gao et al., 2016a; Gao et al., 2016b; Wang et al., 2013; Wang et al., 2014). In light of this, to further enhance the understanding of related

phenomena involved in gap resonance, this paper considers the influences of the topographic variation on the gap resonance problem for the first time. As in Kristiansen and Faltinsen (2009), Tan et al. (2014) and Meringolo et al. (2018), the fluid resonance inside a narrow gap formed between a fixed box and a vertical wall is taken as the background of this study, and the investigations in the current paper are carried out in two-dimensions.

This paper is organized as follows. Section 2 briefly describes the numerical model employed in this work. Section 3 presents the incident wave parameters and the setup of the numerical wave tank. Section 4 validates the numerical model via available laboratory experiments. The numerical results and discussions are presented in Section 5 to show the effects of the seafloor topography on the fluid resonant frequency, the resonant free-surface amplification in the gap and the reflection coefficient of the box-wall system. Concluding remarks based on the results are drawn in Section 6.

2. Numerical model description

To consider the physical energy dissipation near the gap due to the viscous effect, a viscous flow solver is necessary. Similar to Moradi et al. (2015, 2016), Feng et al. (2017), Jiang et al. (2018) and Jiang et al. (2019), the numerical wave tank in this paper is also based on the OpenFOAM® multiphase solver "interFoam" with modifications to incorporate the "waves2Foam" toolbox proposed by Jacobsen et al. (2012) for wave generation and absorption.

2.1. Governing equations

The continuity and Navier-Stokes equations are utilized as the governing equations to solve the two-phase flow of water and air:

$$\frac{\partial \rho}{\partial t} + \nabla \cdot (\rho \mathbf{u}) = 0 , \tag{1}$$

$$\frac{\partial \rho \mathbf{u}}{\partial t} + \nabla \cdot (\rho \mathbf{u}\mathbf{u}^T) = -\nabla P - (\mathbf{g} \cdot \mathbf{x}) \nabla \rho + \nabla \cdot (\mu \nabla \mathbf{u}) + \sigma_t k_\alpha \nabla \alpha , \tag{2}$$

where ρ is the fluid density, $\nabla = \left(\frac{\partial}{\partial x}, \frac{\partial}{\partial y}, \frac{\partial}{\partial z}\right)$ is the gradient operation, $\mathbf{u}=(u, v, w)$ is the velocity vector of the fluid, $\mathbf{x}=(x, y, z)$ is the Cartesian coordinate vector, $\mathbf{g}$ is the gravitational acceleration, P is the pressure in excess of the hydrostatic part, μ is the dynamic viscosity of the fluid, σ_t is the surface tension coefficient and k_α is the surface curvature. The above equations are solved for both water and air simultaneously. Note that $\rho=\rho(\mathbf{x})$ varies with the volume fraction of water α in the computational cell, and the mixed fluid is also tracked by using the scalar field α which takes a

value of 1 for water and 0 for air and intermediate values for a mixture of water and air.

The distribution of α is modelled by the following advection transport equation:

$$\frac{\partial \alpha}{\partial t} + \nabla \cdot (\alpha \mathbf{u}) + \nabla \cdot \left[\alpha (1-\alpha) \mathbf{u}_r \right] = 0, \tag{3}$$

in which $\mathbf{u}_r = \mathbf{u}_{water} - \mathbf{u}_{air}$ is a relative velocity between the water and the air. The last term on the left hand side of the above equation is often referred to as the interface compression term, which limits the smearing of the interface. Briefly, the implementation is based on an explicit first-order time integration routine, and the detailed descriptions of the solution algorithm can be found in Berberović et al. (2009). Using α, the spatial variation of any fluid property φ (e.g., the fluid density ρ and the dynamic viscosity μ) can be expressed through a weighting:

$$\varphi = \alpha \varphi_{water} + (1-\alpha) \varphi_{air}, \tag{4}$$

in which the subscripts "water" and "air" denote the corresponding fluid property of water and air, respectively.

2.2. Boundary conditions and numerical implementations

All the simulations in this paper are carried out by using OpenFOAM® version 3.0.1. The relaxation-based toolbox "waves2Foam" proposed by Jacobsen et al. (2012) is employed to generate and absorb waves at the boundaries (see Fig. 1). At the inlet boundary, the velocity is defined as that of a regular incoming wave, and the pressure gradients are set to zero. A relaxation zone is deployed at the inlet boundary to absorb the reflected waves. The details of the wave-generation method and the relaxation zone technique can be found in Jacobsen et al. (2012). At the upper part of the tank, the boundary condition is set as "atmosphere"; while at the solid walls of the fixed box, the bottom and right boundaries of the tank, "no-slip" boundary condition is applied. For a two-dimensional problem, the boundary condition on the walls in the third dimension is set to "empty".

The governing equations (1)-(2) and the advection transport equation (3) are solved using the finite volume method. The velocity-pressure coupling is resolved using the PISO (Pressure Implicit with Splitting of Operator) algorithm (Jasak, 1996). Gradients are approximated by the Gaussian integration method based on a linear interpolation from cell centers to cell faces. The time derivatives are solved by a first-order Euler scheme. The Gauss Convection-specific schemes are used for the evaluation of the divergence terms. Identical to Feng et al. (2017), in order to produce accurate and stable results, the largest Courant number is set to 0.25 in all simulations.

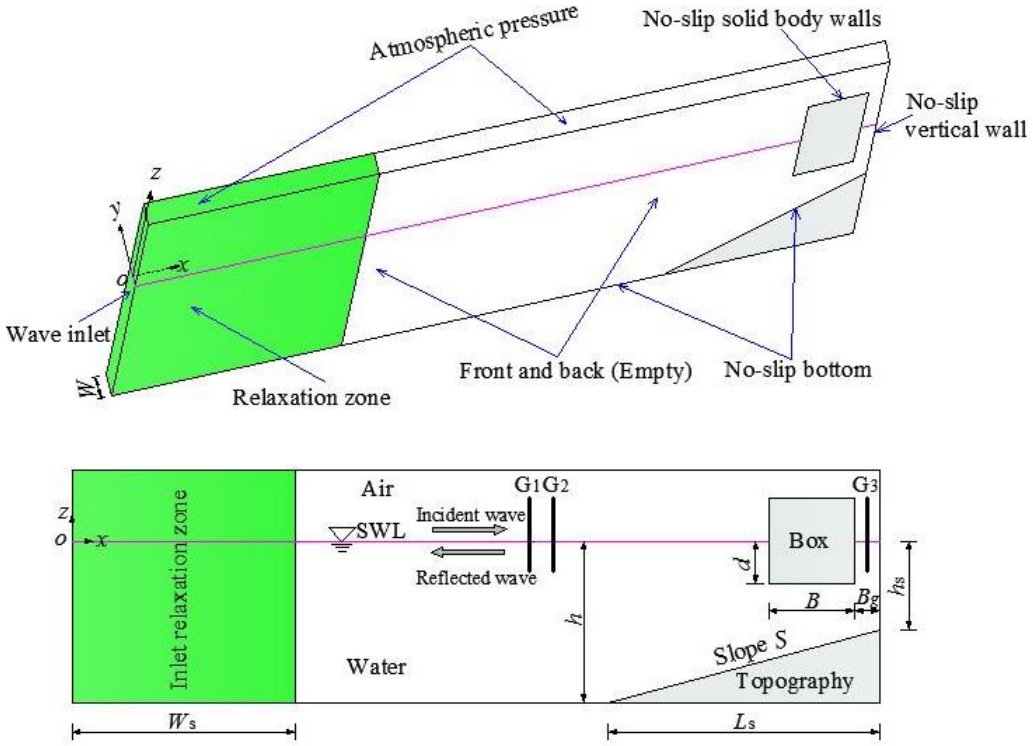

Fig. 1. Sketch of the numerical wave tank: (a) boundary conditions and the definition of the coordinate system; (b) positions of wave gauges and the definition of the geometric parameters.

3. Numerical wave tank

Fig. 1 presents the sketch of the two-dimensional numerical wave tank employed in the current research. The numerical wave tank has a height of 0.8 m, a length of 14.0 m, and a width of W=0.1 m. The Cartesian coordinate system (o, x, y, z) is defined in such a way that the origin is located on the still water level (SWL) of the left inlet boundary; x is in the wave propagation direction and z is in the upward direction. The thickness of the wave tank in the y-axis direction corresponds to one computational cell. A fixed box is placed in the vicinity of the right boundary of the wave tank that acts as a fully reflective vertical wall. The box height is H=0.5 m, the breadth is B=0.5 m, the draft d=0.25 m, the gap width B_g=0.05 m. The air depth is a constant, h_a=0.3 m. The water depth at the region from x=0 to x=12.0 m is also a constant, h=0.5 m. While at the region from x=12.0 m to x=14.0 m, there exists a plane slope underneath the fixed box, and the horizontal length of the plane slope is a constant, L_s=2.0 m. For the water depth in front of the vertical wall, h_s, there are six different values, and they are 0.5 m, 0.45 m, 0.40 m, 0.35 m, 0. 30 m and 0.27 m; the slopes of the plane slope, S, are correspondingly equal to 0, 0.025, 0.050, 0.075, 0.100 and 0.113 (S=0 is viewed

as a special case of the plane slope in this study). For the case of S=0 (i.e., h=h_s=0.5 m), its configuration is in accordance with the physical model experiments in Tan et al. (2014).

Table 1. Physical meanings and magnitudes of all the parameters associated with the set-up of the numerical wave tank

Parameter	Physical meaning	Magnitude
(o, x, y, z)	Cartesian coordinate system	-
B	Breadth of the box	0.5 m
B_g	Width of the gap	0.05 m
d	Draft of the box	0.25 m
H	Height of the box	0.5 m
H_0	Incident wave height	0.005 m, 0.024 m, 0.05 m, 0.075 m, 0.1 m
h_a	Air depth	0.3 m
h	Water depth at the deeper region	0.5 m
h_s	Water depth in front of the vertical wall	0.5 m, 0.45 m, 0.4 m, 0.35 m, 0.3 m, 0.27 m
L_s	Horizontal length of the slope	2.0 m
L	Incident wavelength	From 1.85 m to 5.24 m
kh	Dimensionless wavenumber	From 0.6 to 1.7
S	Topographical slope	0, 0.025, 0.050, 0.075, 0.100, 0.113
ω	Incident wave frequency	From 2.514 rad/s to 5.586 rad/s
W	Width of the numerical wave tank	0.1 m
W_s	Width of the relaxation zone	8.0 m

In the simulations, the incident regular waves with different wave heights and frequencies are generated at the left boundary of the tank. Five different wave heights are considered, which are H_0=0.005 m, 0.024 m, 0.050 m, 0.075 m and 0.100 m. The incident wave frequency, ω, ranges from 2.514 rad/s to 5.586 rad/s. According to the following linear dispersion relationship

$$\omega^2 = gk\tanh(kh), \tag{5}$$

the dimensionless wavenumber, kh, ranges from 0.6 to 1.7, in which k=2π/L denotes the wavenumber and L denotes the incident wavelength. Three wave gauges, G_1-G_3 as shown in Fig. 1, are deployed to record the time histories of free surface elevations at three different locations. Based on the wave analysis technique in Goda and Suzuki (1976), the wave height of the reflected waves from the box-wall system can be obtained by using the free-surface elevations at G_1 and G_2. The

reflection coefficient C_r is further calculated as the ratio of the reflected wave height to the incident wave height H_0. The distance between G_1 and G_2 is set to 0.25 m, and G_2 is arranged at 2.0 m from the toe of the plane slope. G_3 is placed in the middle of the gap to obtain the free surface elevation inside the narrow gap. One relaxation zone of W_s=8.0 m is deployed at the inlet boundary of the wave tank to absorb the reflected waves. The length of 8.0 m is approximately 1.53 times of the maximum wavelength that corresponds to the incident waves with ω=2.514 rad/s. To facilitate the reader's understanding of this paper, all the parameters related to the setup of the numerical wave tank and their physical meanings and magnitudes are listed in Table 1.

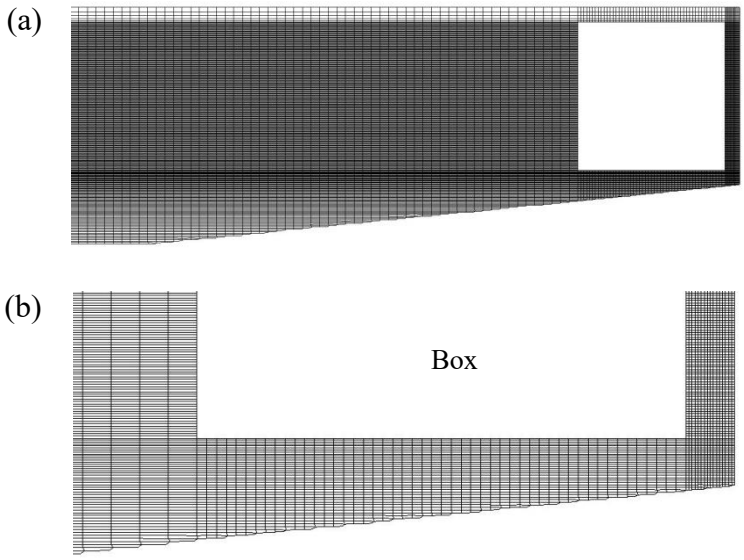

Fig. 2. Side view of typical meshes in the computational domain: (a) the meshes above the topography; (b) the meshes around the box (taking the topography with S = 0.100 as an example)

Two built-in mesh generation utilities supplied by OpenFOAM®, "blockMesh" and "snappyHexMesh", are utilized to generate the meshes. A typical computational mesh is illustrated in Fig. 2, where the topography with S = 0.100 is taken as an example. Non-uniform meshes are adopted for saving the computational time. The fine meshes with higher resolution are employed around the boxes, especially in the vicinity of the narrow gap. In order to accurately capture the motion of the free surface, the mesh density gradually becomes larger from the atmosphere and the bottom boundaries to the still water level.

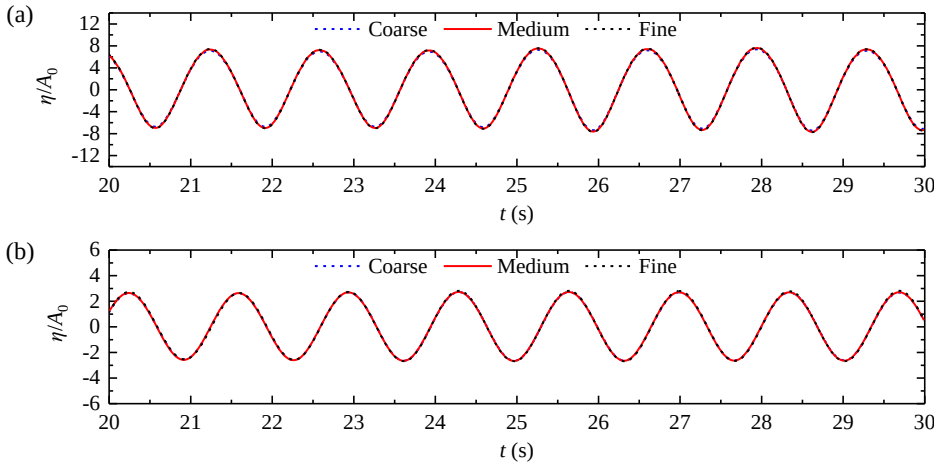

Fig. 3. Dependence of the free-surface elevation in the gap on the mesh resolution for the incident waves with kh=1.286 and H_0=0.024 m, in which A_0= H_0/2 denotes the amplitude of the incident waves. (a) and (b) correspond to the topographies with S = 0 and 0.100, respectively.

Table 2. Details of the coarse, medium and fine meshes for the topography with S=0

Mesh type	No. of cells	No. of points	No. of faces	No. of cells across the gap	
				Along the x-axis	Along the z-axis
Coarse	117,280	238,890	466,243	20	240
Medium	203,890	410,860	817,100	26	280
Fine	281660	566,744	1,128,353	34	330

To check the effects of different mesh resolutions on the numerical result, the response of the free surface inside the narrow gap between the box and the vertical wall is simulated by employing three different meshes, namely the coarse, medium and fine meshes. For the topography with S=0, the details of the three different meshes are listed in Table 2. For the other five topographies with S=0.025, 0.050, 0.075, 0.100 and 0.113, because the mesh underneath the plane slope is removed by snappyHexMesh, the numbers of the cells for these three meshes are slightly less than those for the topography with S=0. According to the numerical results which will be presented in Section 4.1, for the topography with S=0, the free-surface resonance inside the narrow gap occurs at kh=1.286. The resonant free-surface elevations inside the narrow gap excited by the incident waves with kh=1.286 and H_0=0.024 m are illustrated in Fig. 3, in which A_0=H_0/2 denotes the amplitude of the incident waves. Besides, to examine the mesh convergence of the numerical result for the

topography with $S \neq 0$, the free-surface elevations inside the gap induced by the incident waves with the same frequency and wave height under the condition of S=0.100 are also presented in this figure. It is seen that under both conditions of S=0 and 0.100, the time series of the free-surface elevations inside the narrow gap for the three mesh configurations are almost identical to each other, which indicates that the numerical results are insensitive to the selected meshes. Considering that the medium mesh can provide more accurate simulations of the wave fields excited by the incident waves with higher frequencies as compared to the coarse mesh, in all our numerical simulations, the medium mesh configuration is adopted in all numerical simulations.

A total time of 40.0 s is simulated for all the cases. It can be observed from Fig. 3 that the free surface elevation in the narrow gap has already reached a steady state at t=20.0 s. All the numerial results that will be shown in Section 4.1 and Section 5 are based on the simulated steady-state data ranging from 20.0 s to 40.0 s. All simulations are implemented on a Dell Workstation with Intel Xeon E5-2640 CPU and do not use the parallel computing technique. For each case, the computational time of 6 h – 12 h is required, which mainly depends on the frequency and wave height of the incident regular waves.

4. Numerical model validation

To ensure the reliability of the numerical model and the accuracy of the numerical results, the numerical model and the numerical wave tank presented in Sections 2 and 3 are first validated by comparing the present results obtained by OpenFOAM® with available experimental data. For the cases with S=0 and H_0=0.024 m described in Section 3, Tan et al. (2014) have implemented a series of laboratory experiments. Comparisons of the present numerical results with the experimental data of Tan et al. (2014) are presented in Section 4.1. Because this paper mainly focuses on influences of the topographical variation on the gap resonance problem, it is obvious that the incident wave parameters such as wave height would change due to the topographical variation, which would further affect the wave fields around the box and inside the gap. Hence, it is necessary to further validate the capacity of the present numerical model in terms of predicting the wave transformation over an uneven seabed. Ohyama et al. (1995) conducted a set of physical experiments for wave evolutions during passage over a submerged bar under various wave conditions. The numerical reproductions for part of their experiments are carried out in Section 4.2.

4.1. Validation of gap resonance

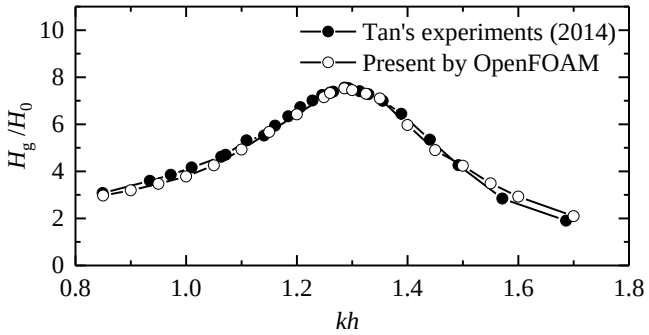

Fig. 4. Amplification of the free-surface elevation inside the narrow gap for the cases with S=0 and H_0=0.024 m, in which H_g denotes the wave height inside the narrow gap.

Fig. 4 presents the amplification of the free-surface elevation inside the narrow gap induced by the incident waves with H_0=0.024 m for the cases with S=0. H_g in this figure denotes the wave height inside the narrow gap. It is seen that the predicted resonant frequency, kh=1.286, by the present numerical model is identical to that obtained by the laboratory experiments of Tan et al. (2014) (i.e., the resonant period of 1.35 s). Moreover, the overall variation of H_g/H_0 with respect to kh also agrees well between the numerical and experimental results.

Fig. 5 illustrates the comparison of the wave height inside the gap predicted by OpenFOAM® and those measured by Tan et al. (2014) when the gap is exposed to a set of incident waves with kh=1.286 and various wave heights. Based on the experimental data, Tan et al. (2014) obtained a fitted curve to describe the variation of the wave height inside the gap:

$$H_g = 10.16 H_0^{0.64} \tag{6}$$

The units of both H_0 and H_g used in the above equation are centimeter. It can be observed from this figure that the numerical results agree well with both the experimental data and the fitted curve of Tan et al. (2014). It is also clear that the relative damping of the box-wall system considerably increases with the incident wave height, which is due to the effects of vortex shedding and flow separation at the bottom corner of the box. Fig. 6 presents the velocity vectors around the lower right corner of the box at t=30.25 s for the three cases with H_0=0.005 m, 0.03 m and 0.05 m. The time instant t=30.25 s corresponds to the time when the free surface elevation in the gap is at its

mean level near zero and the fluid is moving upward with the maximum velocity. It is clear that the larger the incident wave height is, the more obvious the vortex shedding and the flow separation around the corner become.

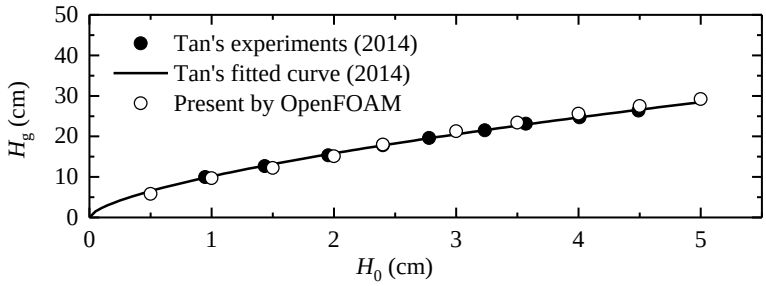

Fig. 5. Variation of the wave height in the narrow gap with respect to the incident wave height for the cases with S=0 and kh=1.286.

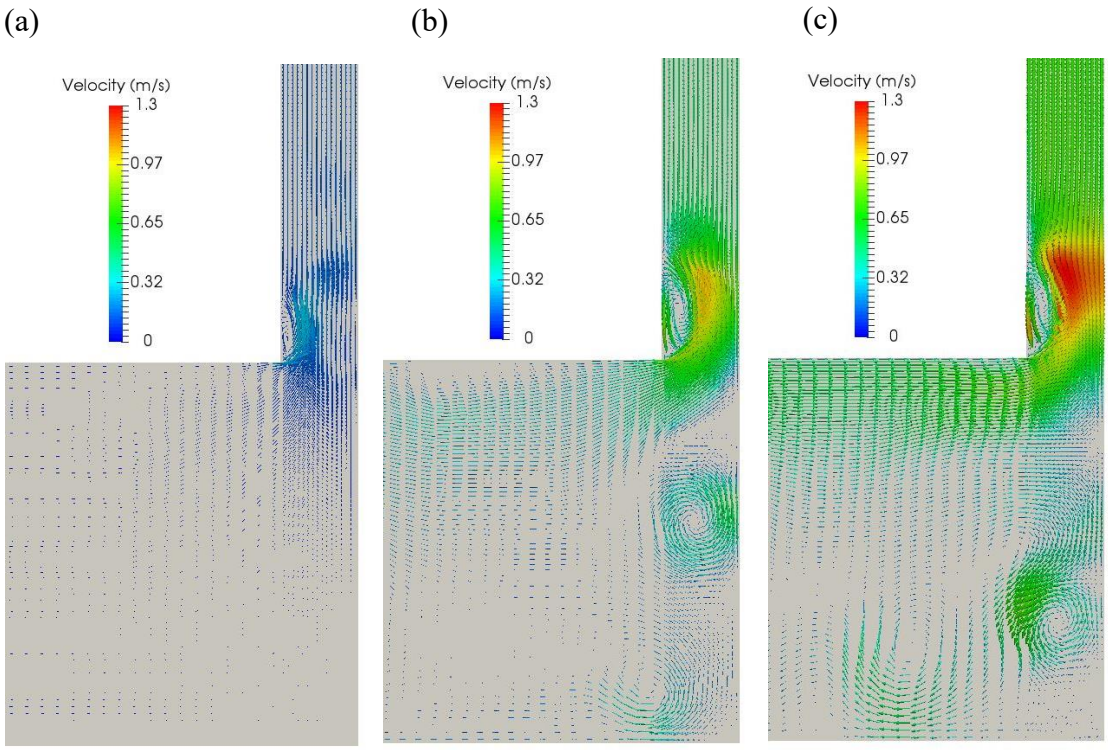

Fig. 6. Velocity vectors around the bottom corner of the box at t=30.25 s. (a)-(c) correspond to the cases with H_0=0.005 m, 0.03 m and 0.05 m, respectively.

As Tan et al. (2014) pointed out, the reflection coefficient is useful for evaluating the energy dissipation due to the fluid resonance between the box and the vertical wall. Hence, it is also necessary to further examine the capacity of the numerical model to predict the reflection coefficient.

Fig. 7 shows the comparison of the reflection coefficient C_r predicted by OpenFOAM® and those measured by Tan et al. (2014) for the cases with S=0 and H_0=0.024 m. Similar to Figs. 4 and 5, the overall agreement between the numerical results and the measured data in Tan et al. (2014) is also observed. This demonstrates that the numerical wave tank shown in Fig. 1 and the medium mesh described in Section 3 can obtain accurate and reliable numerical results for the gap resonance problem formed by the fixed box in front of the vertical wall.

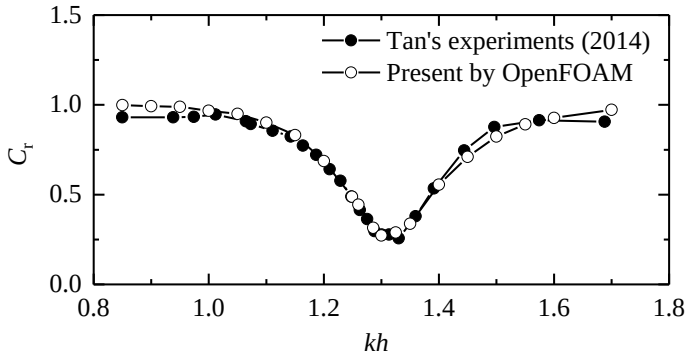

Fig. 7. Reflection coefficient C_r for the cases with S=0 and H_0=0.024 m

4.2. Validation of wave transformation on submerged bar

Ohyama et al. (1995) performed physical model experiments in a wave tank with a length of 65 m, a width of 1.0 m, and a height of 1.6 m. The configuration of a submerged trapezoidal bar adopted in their experiments and the location of the wave gauges are shown in Fig. 8. The still water depths in the deeper region and over the horizontal part of the submerged bar were 0.50 m and 0.15 m, respectively. The distance from the center of the bar to a piston-type wave generator, fixed at one end of the tank, was 28.3 m. A wave absorber, formed by coarse material, was arranged at the other end of the tank. In the physical experiments, six wave conditions were considered, emerging from the combination of two wave heights with three wave periods. In this paper, only the incident regular waves with the larger wave height are simulated (H_0/h_0=0.1), which results in a total of three wave conditions, i.e. Cases 2, 4 and 6 in Ohyama et al. (1995) with the wave periods of $T_0(g/h)^{1/2}$= 5.94, 8.91 and 11.88, respectively.

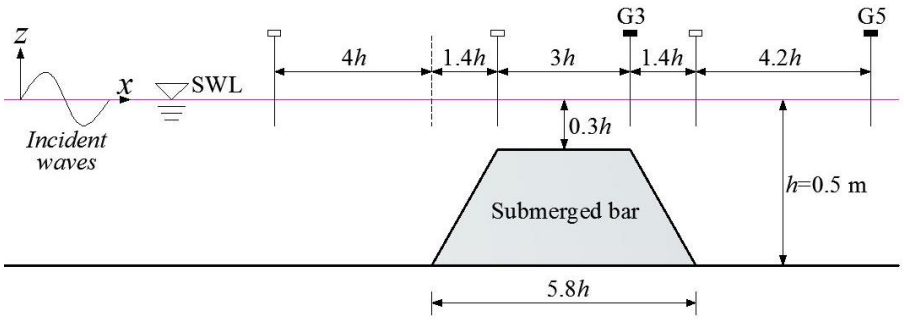

Fig. 8. Configuration of submerged trapezoidal bar and locations of wave gauges in the physical experiments of Ohyama et al. (1995).

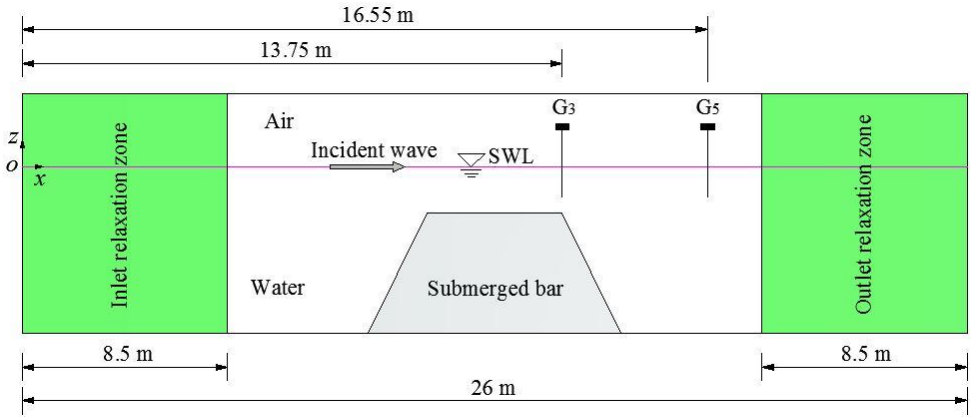

Fig. 9. Sketch of the numerical wave tank for the experiments of Ohyama et al. (1995).

Fig. 9 illustrates the sketch of the two-dimensional numerical wave tank used for reproducing the experiments of Ohyama et al. (1995). Due to the employment of the relaxation technique, the length of the numerical wave tank can be greatly reduced comparing with that of the physical wave tank. The numerical wave tank has a length of 26.0 m and a height of 0.8 m. The submerged bar is placed at the middle of the wave tank. Similar to the numerical wave tank shown in Fig. 1, the air depth is 0.3 m and the water depth at the deeper region is 0.5 m. Two relaxation zones of 8.5 m long each are arranged at the inlet and outlet boundaries of the wave tank to absorb the reflected and transmitted waves. The length of 8.5 m is equal to 1.50 times of the maximum wavelength that corresponds to the incident waves with $T_0(g/h)^{1/2}$=11.88, which guarantees a good wave-absorbing performance for the two relaxation zones (Jacobsen et al., 2012). Because only the time series of the free surface elevations at Gauges 3 and 5 were presented in Ohyama et al. (1995), only these two gauges are deployed in the numerical wave tank, and their distances to the wave inlet boundary are 13.75 m and 16.55 m, respectively. Considering that water depth in the deeper region and the

height of the numerical tank shown in Fig. 9 are identical to those in Fig. 1, a mesh configuration that has a similar mesh density with the medium mesh described in Section 3 is adopted.

Fig. 10 presents the comparisons of the experimental and simulated time-series of the free-surface elevations at Gauges 3 and 5 for Cases 2, 4 and 6. For both gauges, very good agreement between the experimental and numerical results is observed. Similar to Morgan and Zang (2011), the nonlinear wave transformation (such as obvious high-order wave components) during passage over the submerged bar is well captured by the OpenFOAM® model. It proves that the numerical model is able to accurately simulate the evolution of the wave fields over varying topography.

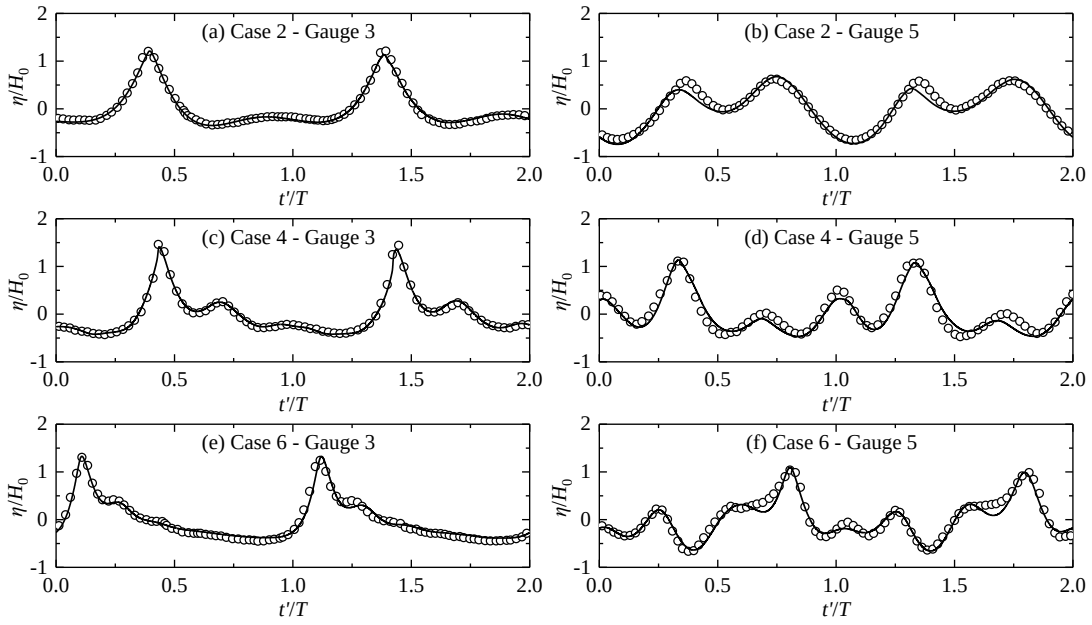

Fig. 10. Comparison of the present results by OpenFOAM® (lines) and experimental data of Ohyama et al. (1995) (circles) for the free-surface elevations at Gauges 3 and 5 in Cases 2, 4 and 6

5. Numerical results and discussion

The validation investigations in the previous section illustrate that the present numerical wave tank can accurately reproduce the studied scenario of gap resonance between a fixed box and a vertical wall, and the numerical model is able to well simulate the wave transformation over uneven topography. They are further used to study the effects of the topographical variation on the fluid resonance in the narrow gap formed by the fixed box in front of the vertical wall under wave actions. As mentioned in Section 3, the plane slopes with S=0, 0.025, 0.050, 0.075, 0.100 and 0.113 and the

incident regular waves with H_0=0.005m, 0.024 m, 0.050 m, 0.075 m and 0.100 m are considered herein (refer to Table 1). Numerical results include the amplification of the free-surface elevation in the narrow gap for all cases, and the variations of the fluid resonant frequency, the resonant wave height and the reflection coefficient under the gap-resonance condition with respect to the topographical slope and the incident wave height.

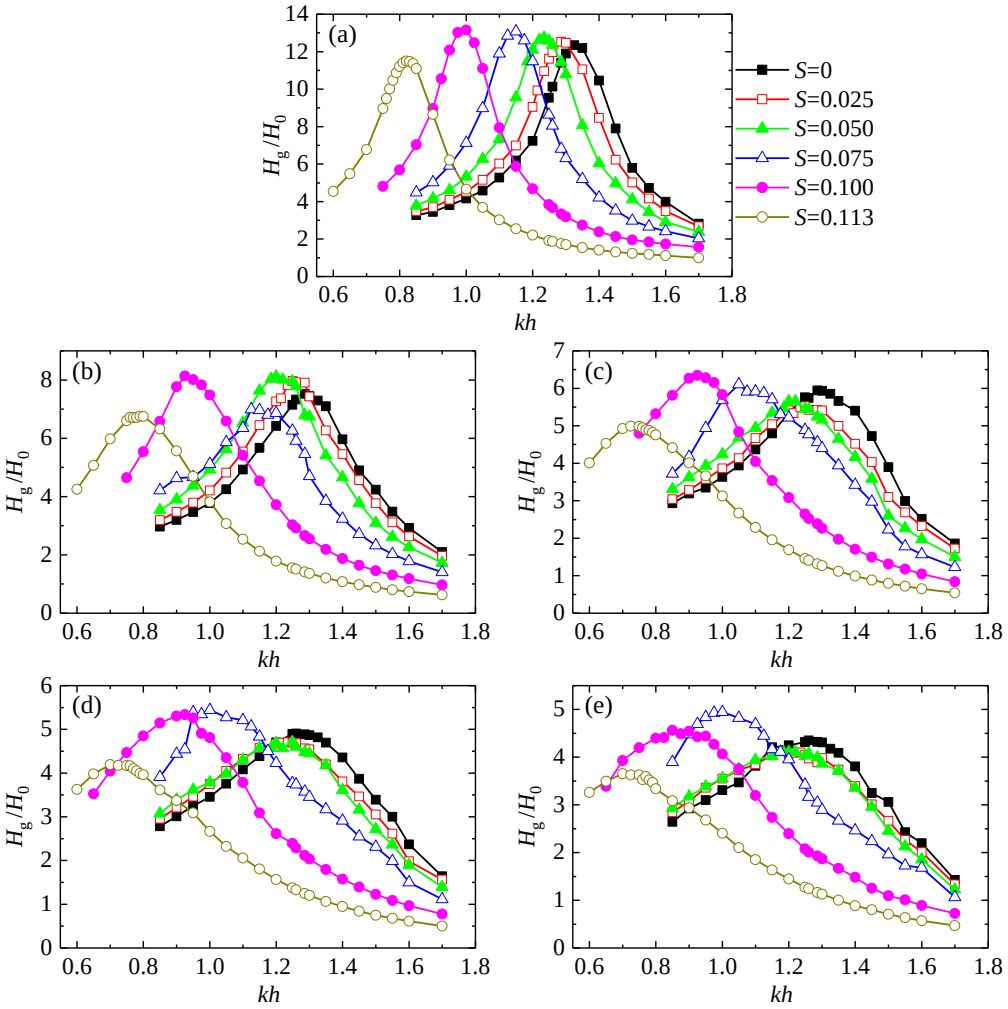

Fig. 11. The amplification of the free-surface elevation in the gap excited by the incident regular waves with various wave heights. (a)-(e) correspond to H_0=0.005 m, 0.024 m, 0.050 m, 0.075 m and 0.100 m, respectively.

Fig. 11 shows the amplification of the free-surface elevation inside the narrow gap induced by the incident regular waves with various wave heights. There are two obvious phenomena that can be intuitively observed from this figure. First, for all the incident wave heights considered in this

paper, the fluid resonant frequency inside the narrow gap always decreases with the increase of the topographical slope, S. Second, for each topography, the maximum wave amplification inside the gap gradually decreases as the incident wave height increases. These two phenomena and other more phenomena related to the fluid resonance in the gap will be revealed and analyzed in detail in the following.

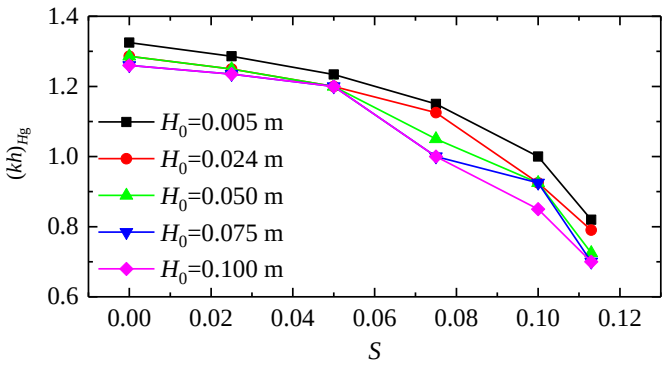

Fig. 12. The variation of the fluid resonant frequency, $(kh)_{Hg}$, with respect to the topographical slope, S.

In order to better present the first phenomenon shown in Fig. 11, the variation of the fluid resonant frequency, $(kh)_{Hg}$, with respect to the topographical slope, S, is further presented in Fig. 12. It is seen that the fluid resonant frequency decreases monotonously with the topographical slope, and in general, the decreasing rate of the fluid resonant frequency is aggravated as the topographical slope increases. These findings are similar to those by Moradi et al. (2016) who conducted a series of two-dimensional numerical simulations to investigate the effect of water depth on resonance behavior of the fluid trapped between two side-by-side bodies, although the bottoms of the numerical tank employed in Moradi et al. (2016) are always flat and the variation of the water depth refers to its variation in the whole water domain. In the current study, the increase of the topographical slope results in the decrease of the local water depth beneath the gap. Hence, it can be further concluded that in shallow and transitional water regimes, only the reduction of the local water depth under the narrow gap can lead to the notable decease of the fluid resonant frequency, and it is not necessary to reduce the water depth in the whole water domain.

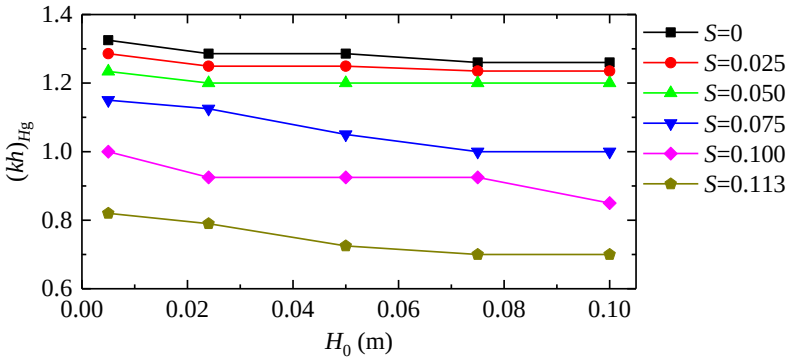

Fig. 13. The variation of the fluid resonant frequency, $(kh)_{Hg}$, with respect to the incident wave height, H_0.

Table 3. Comparisons of the fluid resonant frequency, $(kh)_{Hg}$, under the conditions of H_0=0.005 m and 0.100 m for all the topographies considered in this paper. Ψ in the table denotes the declining rate of $(kh)_{Hg}$ when H_0 increases from 0.005 m to 1.000 m.

$(kh)_{Hg}$ / H_0 (m) \ S	0	0.025	0.050	0.075	0.100	0.113
0.005	1.325	1.286	1.234	1.150	1.000	0.820
0.100	1.260	1.235	1.200	1.000	0.850	0.700
Ψ (%)	4.91	3.97	2.76	13.04	15.00	14.63

0 0.025 0.050 0.075 0.100 0.113
0.005 1.325 1.286 1.234 1.150 1.000 0.820
0.100 1.260 1.235 1.200 1.000 0.850 0.700
Ψ (%) 4.91 3.97 2.76 13.04 15.00 14.63

By further observing Fig. 12, it can also be found that for all the topographies considered in this paper, the fluid resonant frequency is affected by the incident wave height as well, especially for the topographies with larger slopes. Fig. 13 shows the variations of the fluid resonant frequency, $(kh)_{Hg}$, with respect to the incident wave height, H_0. For all the topographies considered in this paper, the fluid resonant frequency exhibits different degrees of downward tendencies with the increase of the incident wave height. It can be seen that in general the declining degrees of the fluid resonant frequency for the topographies with smaller slopes are relatively small, while these for the topographies with larger slopes become much larger. To better illustrate this phenomenon, Table 3 presents the quantitative comparisons of the fluid resonant frequencies under the conditions of H_0=0.005 m and 0.100 m. When the incident wave height increases from 0.005 m to 0.100 m, for the topographies with S=0, 0.025 and 0.050, the declining rates of the fluid resonant frequencies are 4.91%, 3.97% and 2.76%, respectively. While for the other three topographies with S=0.075, 0.100 and 0.113, the declining rates of the fluid resonant frequencies reach up to 13.04%, 15.00% and

14.63%, respectively.

The above findings are different from those by Feng and Bai (2015) who found that the fluid resonant frequency for the piston mode shifts slightly to a higher frequency as the wave steepness increases. This difference may be caused by the following two reasons. First, the configurations of the gap resonance problem are different in the present paper and in Feng and Bai (2015). In this paper, the narrow gap is formed by a box and a vertical wall; while in Feng and Bai (2015), the narrow gap was formed between two side-by-side three-dimensional barges. For the former, except that part of the wave energy is dissipated around the box and inside the gap, the incident waves can only be reflected from the box-wall system. For the latter, part of the incident wave energy can also be transmitted through the two barge system and be radiated from the two ends of the gap. Second, the numerical models employed in these two papers are different. A fully nonlinear potential flow model was employed in Feng and Bai (2015). As stated in the Introduction, the energy dissipation caused by the fluid viscosity, vortex shedding and turbulence cannot be considered in the context of the potential flow theory. On the contrary, the energy dissipation caused by them is automatically accounted for by the OpenFOAM® model used in this paper.

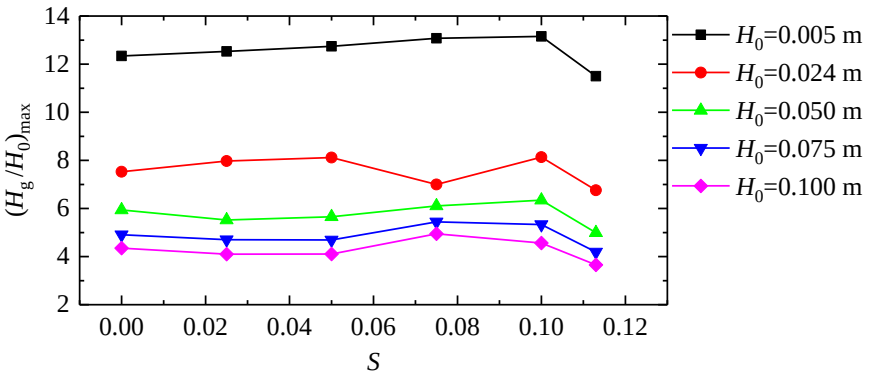

Fig. 14. The variation of the amplification of resonant wave height, $(H_g/H_0)_{max}$, with respect to the topographical slope, S.

Fig. 14 illustrates the variations of the amplification of resonant wave height, $(H_g/H_0)_{max}$, with respect to the topographical slope, S. It is seen that for all the incident wave heights considered in this paper, the amplification of resonant wave height presents a pattern of fluctuation with the topographical slope. This is different from the related finding in Moradi et al. (2016) who found that for a given body draft and gap width, the amplification of the resonant wave height gradually

increase with the decrease of the water depth. As mentioned above, in Moradi et al. (2016), the bottoms of the numerical tank employed in their study are always flat and the variation of the water depth refers to its variation in the whole water domain. While in the current study, the topographies with various slopes change the local water depth underneath the box and the gap. There are two different factors that jointly determine the amplification of resonant wave height inside the gap. On one hand, the shoaling effect of the incident waves over the plane slope tends to intensify the resonant wave height. On the other hand, due to the existence of the slope, the perpendicular distance from the lower right corner of the box to the bottom of the flume becomes small, which can hinder the transmission of the incident wave energy into the gap and decrease the resonant wave height. Hence, the fluctuation of the amplification of resonant wave height with the topographical slope shown in this figure is attributed to the combined effects of these two factors. It is noteworthy that for each incident wave height, the minimum value of $(H_g/H_0)_{max}$ always occurs under the condition of S=0.113, where the local water depth in front of the vertical wall is h_s=0.27 m. Comparing with the draft of the box d=0.25 m, it can be found that the perpendicular distance from the lower right corner of the box to the slope is extremely small (about 2.0 cm). Under this condition, obvious vortex shedding and flow separation near the box and inside the gap is expected, which results in significant energy dissipation.

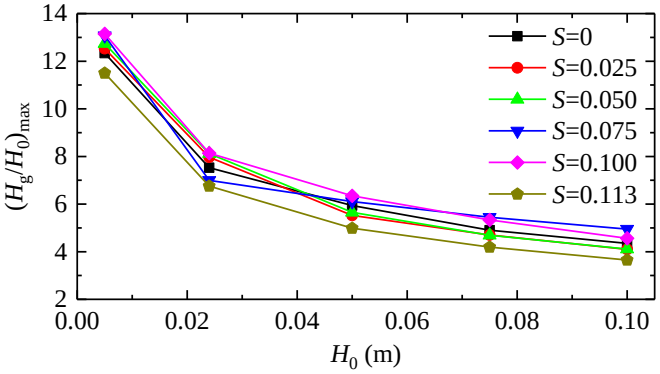

Fig. 15. The variation of the amplification of resonant wave height, $(H_g/H_0)_{max}$, with respect to the incident wave height, H_0.

Fig. 15 further presents the variation of the amplification of resonant wave height, $(H_g/H_0)_{max}$, with respect to the incident wave height, H_0. For all the topographies studied in this paper, the amplification of resonant wave height decrease gradually with the increase of the incident wave

height. It is probably because in general the larger incident wave height results in larger wave reflection from the box-wall system (this will be shown in the following). The portion of the wave energy that transmits into the gap correspondingly decreases with the incident wave height. Hence, the amplification of resonant wave height inside the gap decreases as the incident wave height increases. Besides, it can also be seen that as the incident wave height increases, the decreasing rate of the amplification of resonant wave height gradually decreases. A possible reason for this will be presented in the following.

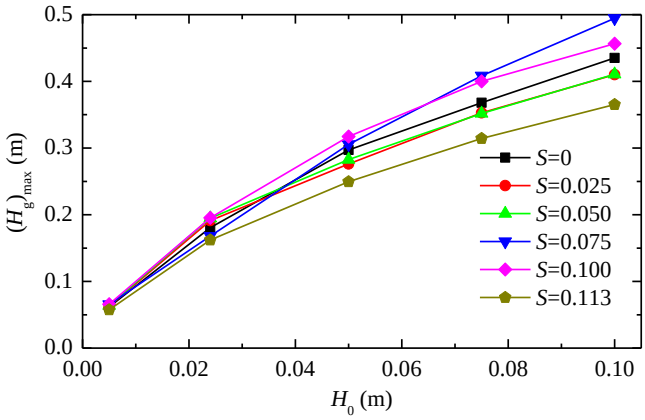

Fig. 16. The variation of the resonant wave height, $(H_g)_{max}$, with respect to the incident wave height, H_0.

If a train of incident waves has a large wave height and excites the fluid resonance inside the gap, the resonant fluid is expected to possess a very large free-surface elevation, which would probably result in wave overtopping on the ship deck or on the wharf. Hence, apart from the amplification of the resonant wave height discussed above, from the viewpoint of wave overtopping, it is also essential to further examine the resonant wave heights inside the narrow gap for all cases. Fig. 16 presents the variation of the resonant wave height, $(H_g)_{max}$, with respect to the incident wave height, H_0, under the conditions of various topographies. As expected, for all the topographies considered in this paper, the resonant wave height increases monotonously with the increase of the incident wave height. Besides, it is also seen that the resonant wave heights for the slope S=0.113 are always less than those for the other four slopes. Hence, from the viewpoint of wave overtopping, the topography with S=0.113 is the safest seabed for all the incident wave heights. Moreover, it can also be found that when the incident wave height is relatively small (i.e., H_0=0.005 m, 0.024 m and

0.050 m), the slope S=0.100 always results in the largest resonant wave height inside the gap. However, when the incident wave height becomes larger (i.e., H_0=0.075 m and 0.100 m), the largest resonant wave height inside the gap always appears at the slope S=0.075. These indicate that from the viewpoint of wave overtopping, the topographies with S=0.100 and S=0.075 are the most dangerous seabeds for relatively small incident wave heights and for larger incident wave heights, respectively.

In order to demonstrate more hydrodynamic characteristics related to the gap resonance, the reflection coefficients of the box-wall system for all the cases in which the gap resonance occurs are further analyzed. Fig. 17 presents the variation of the reflection coefficient under the gap-resonance condition, C_r, with respect to the topographical slope, S. It is seen that similar to the amplification of resonant wave height shown in Fig. 14, the reflection coefficient under the gap-resonance condition also shows a pattern of fluctuation with the topographical slope. This fluctuation characteristic is mainly due to the reflection of the incident waves on the topography. Suh et al. (1997) investigated a train of regular waves propagating over plane slopes with different inclinations by using two time-dependent equations, and the reflection coefficient in front of these plane slopes was systematically analyzed. Obvious fluctuation of the reflection coefficient with respect to the topographical slope was found in their study. Subsequently, this finding was further confirmed by Madsen et al. (2006), Yao et al. (2012) and Gao et al. (2017; 2019b).

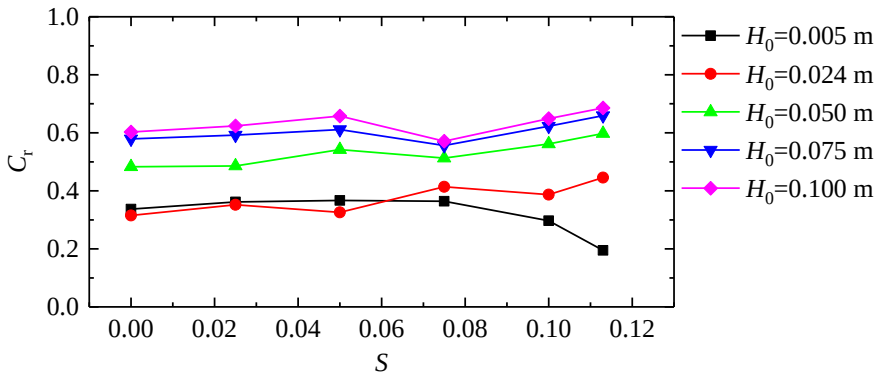

Fig. 17. The variation of the reflection coefficient under the gap-resonance condition, C_r, with respect to the topographical slope, S.

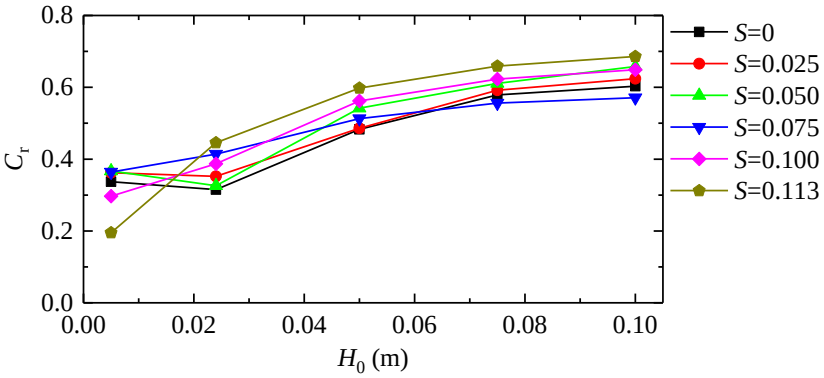

Fig. 18. The variation of the reflection coefficient under the gap-resonance condition, C_r, with respect to incident wave height, H_0.

Fig. 18 further shows the variation of the reflection coefficient under the gap-resonance condition, C_r, with respect to incident wave height, H_0. It can be seen from this figure that the variation trend of the reflection coefficient with the incident wave height depends on the topographical slope. Specifically speaking, when the topographical slope is relatively small (i.e., S=0, 0.025 and 0.050), the value of C_r decreases slightly first and then increase remarkably with the increase of the incident wave height; while for the topographies with larger slopes (i.e., S=0.075, 0.100 and 0.113), the former is shown to increase gradually with the increase of the latter. Moreover, it can also be observed that at the range of $H_0 \geq 0.024$ m, although the reflection coefficients for all the topographies increase with the incident wave height, all of their increasing rates gradually decrease as the incident wave height increases. It can be further inferred that the decreasing rate of the portion of the wave energy that transmits into the gap gradually decreases with the incident wave height, which probably explains the phenomenon shown in Fig. 15 that the decreasing rate of the amplification of resonant wave height gradually decreases with the incident wave height.

6. Conclusions

The CFD-based numerical model, OpenFOAM®, is employed to investigate the hydrodynamic behaviors of fluid resonance inside a narrow gap between a fixed box and a vertical wall induced by the incident regular waves with various wave heights. The “waves2Foam” toolbox, proposed by Jacobsen et al. (2012), is adopted to generate and absorb waves in the numerical wave tank. Compared to the previous investigations, the influences of the topographical variation on the gap

resonance are investigated for the first time in this paper. The capacities of the numerical model to accurately reproduce the gap resonance and the wave transformation over varying topography are firstly validated by using the experimental data of Tan et al. (2014) and Ohyama et al. (1995), respectively. Then, the effects of the topographical variation on the fluid resonance, including the fluid resonant frequency, the resonant wave height in the gap and the reflection coefficient from the box-wall system under the gap-resonance condition, are systematically investigated. The results of this study have provided new insights of the hydrodynamic characteristics involved in the fluid resonance inside the gap formed by large vessels berthing in front of wharfs.

The following conclusions can be drawn from the results of the present study:

1. For all the incident wave heights considered in this paper, the fluid resonant frequency, $(kh)_{Hg}$, decreases monotonously with the topographical slope, and the decreasing rate of the fluid resonant frequency is aggravated as the topographical slope increases overall. Besides, for all the topographies studied in this paper, the fluid resonant frequency is also shown to gradually decrease with the incident wave height, and the decreasing degree depends on the topographical slope. For the topographies with smaller slopes (i.e., S=0, 0.025 and 0.050), the declining rate of the fluid resonant frequency is relatively small (2.76-4.91%); while for the topographies with larger slopes (i.e., S=0, 0.025 and 0.050), the declining rate of the fluid resonant frequency become significantly increased (up to 13.04-15.00%).
2. For all the incident wave height considered in this paper, due to the influence of the wave transformation over the topography, the amplification of the resonant wave height, $(H_g/H_0)_{max}$, presents a pattern of fluctuation with the topographical slope. In addition, for all the topographies studied in this paper, the amplification of the resonant wave height decreases gradually with the increase of the incident wave height, and the declining rate of the former is also shown to gradually decrease with the increase of the latter.
3. From the viewpoint of wave overtopping on the ship deck or on the wharf, the topography with S=0.113 is the safest seabed for all the incident wave heights considered in this paper. While the most dangerous topography depends on the incident wave height. The topographies with S=0.100 and S=0.075 are most dangerous for relatively small incident wave heights and for larger incident wave heights, respectively.
4. The reflection coefficient under the gap-resonance condition is always shown to fluctuate with

respect to the topographical slope. Besides, the variation trend of the reflection coefficient with respect to the incident wave height also depends on the topographical slope. When the slope is relatively small (i.e., S=0, 0.025 and 0.050), the reflection coefficient decreases slightly first and then increase remarkably with the increase of the incident wave height; while for the topographies with larger slopes (i.e., S=0.075, 0.100 and 0.113), the former is shown to increase gradually with the latter.

Finally, we reaffirm here that these conclusions are only valid for the given geometric layout (including the size and draft of the box, the gap width and the water depth) and the ranges of the incident wave height and the topographical slope studied in this paper.

Acknowledgments

This research is financially supported by the National Key Research and Development Program (2017YFC1404200), the National Natural Science Foundation of China (Grant no. 51609108) and the Jiangsu Government Scholarship for Overseas Studies (awarded to Dr. Junliang Gao for study abroad at the University of Bath). The authors also thank UK EPSRC and the Royal Academy of Engineering for providing partial support for this work within the UK-China joint projects ResIn (EPSRC Grant No. EP/R007519/1) and the UK-CIAPP (RAE Grant No. UK-CIAPP/73).

References

Berberović, E., Hinsberg, N.P.v., Jakirlić, S., Roisman, I.V., Tropea, C., 2009. Drop impact onto a liquid layer of finite thickness: Dynamics of the cavity evolution. Physical Review E 79 (3), 036306.

Chen, X.B., 2004. Hydrodynamics in Offshore and Naval Applications (Keynote lecture), The 6th International Conference on Hydrodynamics, Perth, Austrilia.

Clauss, G.F., Dudek, M., Testa, D., 2013. Gap Effects at Side-by-Side LNG-Transfer Operations, Proceedings of the 32nd International Conference on Ocean, Offshore and Arctic Engineering, Nantes, France. Paper No. OMAE2013-10749.

Feng, X., Bai, W., 2015. Wave resonances in a narrow gap between two barges using fully nonlinear numerical simulation. Applied Ocean Research 50, 119-129.

Feng, X., Bai, W., Chen, X.B., Qian, L., Ma, Z.H., 2017. Numerical investigation of viscous effects on the gap resonance between side-by-side barges. Ocean Engineering 145, 44-58.

Gao, J., Ji, C., Liu, Y., Gaidai, O., Ma, X., Liu, Z., 2016a. Numerical study on transient harbor oscillations induced by solitary waves. Ocean Engineering 126, 467-480.

Gao, J., Ji, C., Liu, Y., Ma, X., Gaidai, O., 2017. Influence of offshore topography on the amplification of infragravity oscillations within a harbor. Applied Ocean Research 65, 129-141.

Gao, J., Ma, X., Dong, G., Wang, G., Ma, Y., 2016b. Numerical study of transient harbor resonance induced by solitary waves. Proc IMechE Part M: Journal of Engineering for the Maritime Environment 230 (1), 163–176.

Gao, J., Zang, J., Chen, L., Chen, Q., Ding, H., Liu, Y., 2019a. On hydrodynamic characteristics of gap resonance between two fixed bodies in close proximity. Ocean Engineering 173, 28-44.

Gao, J., Zhou, X., Zhou, L., Zang, J., Chen, H., 2019b. Numerical investigation on effects of fringing reefs on low-frequency oscillations within a harbor. Ocean Engineering 172, 86-95.

Goda, Y., Suzuki, T., 1976. Estimation of incident and reflected waves in random wave experiments, Proceedings of the 15th Coastal Engineering Conference, Honolulu, Hawaii, pp. 828-845.

Huijsmans, R.H.M., Pinkster, J.A., Wilde, J.J.d., 2001. Diffraction and radiation of waves around side-by-side moored vessels, Proceedings of the Eleventh (2001) International Offshore and Polar Engineering Conference, Stavanger, Norway. Paper No. ISOPE-I-01-061., pp. 406-412.

Iwata, H., Saitoh, T., Miao, G., 2007. Fluid resonance in narrow gaps of very large floating structure composed of rectangular modules, Proceedings of the 4th International Conference on Asian and Pacific Coasts, Nanjing, China, pp. 815-826.

Jacobsen, N.G., Fuhrman, D.R., Fredsøe, J., 2012. A wave generation toolbox for the open-source CFD library: OpenFoam®. International Journal for Numerical Methods in Fluids 70 (9), 1073-1088.

Jasak, H., 1996. Error Analysis and Estimation in the Finite Volume Method with Applications to Fluid Flows. PhD thesis, Imperial College, London.

Jiang, S.-C., Bai, W., Cong, P.-W., Yan, B., 2019. Numerical investigation of wave forces on two side-by-side non-identical boxes in close proximity under wave actions. Marine Structures 63, 16-44.

Jiang, S.-C., Bai, W., Tang, G.-Q., 2018. Numerical simulation of wave resonance in the narrow gap between two non-identical boxes. Ocean Engineering 156, 38-60.

Kristiansen, T., Faltinsen, O.M., 2009. Studies on resonant water motion between a ship and a fixed terminal in shallow water. Journal of Offshore Mechanics and Arctic Engineering 131 (2), 021102.

Li, B., Cheng, L., J.Deeks, A., Teng, B., 2005. A modified scaled boundary finite-element method for

problems with parallel side-faces. Part II. Application and evaluation. Applied Ocean Research 27 (4-5), 224-234.

Li, X., Xu, L.-y., YANG, J.-m., 2016. Study of fluid resonance between two side-by-side floating barges. Journal of Hydrodynamics, Ser. B 28 (5), 767-777.

Li, Y., Zhang, C., 2016. Analysis of wave resonance in gap between two heaving barges. Ocean Engineering 117, 210-220.

Liu, Y., Li, H.-j., 2014. A new semi-analytical solution for gap resonance between twin rectangular boxes. Proc IMechE Part M: Journal of Engineering for the Maritime Environment 228 (1), 3-16.

Lu, L., Teng, B., Cheng, L., Sun, L., Chen, X., 2011a. Modelling of multi-bodies in close proximity under water waves—Fluid resonance in narrow gaps. Science China Physics, Mechanics and Astronomy 54 (1), 16-25.

Lu, L., Teng, B., Sun, L., Chen, B., 2011b. Modelling of multi-bodies in close proximity under water waves—Fluid forces on floating bodies. Ocean Engineering 38 (13), 1403-1416.

Madsen, P.A., Fuhrman, D.R., Wang, B., 2006. A Boussinesq-type method for fully nonlinear waves interacting with a rapidly varying bathmetry. Coastal Engineering 2006, 487-504.

Meringolo, D.D., Liu, Y., Lu, L., 2018. Energy Analysis of Wave Resonance in a Gap through an SPH Model, Proceedings of the Twenty-eighth (2018) International Ocean and Polar Engineering Conference, Sapporo, Japan. Paper No. ISOPE-I-18-239,, pp. 338-344.

Miao, G., Ishida, H., Saitoh, T., 2000. Influence of gaps between multiple floating bodies on wave forces. China Ocean Engineering 14 (4), 407-422.

Miao, G., Saitoh, T., Ishida, H., 2001. Water wave interaction of twin large scale caissons with a small gap between. Coastal Engineering Journal 43 (1), 39-58.

Molin, B., 2001. On the piston and sloshing modes in moonpools. Journal of Fluid Mechanics 430, 27-50.

Molin, B., Remy, F., Kimmoun, O., Stassen, Y., 2002. Experimental study of the wave propagation and decay in a channel through a rigid ice-sheet. Applied Ocean Research 24 (5), 247-260.

Moradi, N., Zhou, T., Cheng, L., 2015. Effect of inlet configuration on wave resonance in the narrow gap of two fixed bodies in close proximity. Ocean Engineering 103, 88-102.

Moradi, N., Zhou, T., Cheng, L., 2016. Two-dimensional numerical study on the effect of water depth on resonance behaviour of the fluid trapped between two side-by-side bodies. Applied Ocean Research

58, 218-231.

Morgan, G.C.J., Zang, J., 2011. Application of OpenFOAM to Coastal and Offshore Modelling, Proceedings of the 26th International Workshop on Water Waves and Floating Bodies, Athens, Greece.

Newman, J.N., 2004. Progress in wave load computations on offshore structures (Invited lecture), The 23th Conference on Offshore Mechanics and Arctic Engineering (OMAE2004), New York, USA.

Ning, D., Su, X., Zhao, M., 2016. Numerical investigation of solitary wave action on two rectangular boxes with a narrow gap Acta Oceanologica Sinica 35 (12), 89-99.

Ning, D., Su, X., Zhao, M., Teng, B., 2015a. Hydrodynamic difference of rectangular-box systems with and without narrow gaps. Journal of Engineering Mechanics 141 (8), 04015023.

Ning, D., Su, X., Zhao, M., Teng, B., 2015b. Numerical study of resonance induced by wave action on multiple rectangular boxes with narrow gaps. Acta Oceanologica Sinica 34 (5), 92-102.

Ning, D., Zhu, Y., Zhang, C., Zhao, M., 2018. Experimental and numerical study on wave response at the gap between two barges of different draughts. Applied Ocean Research 77, 14-25.

Ohyama, T., Kioka, W., Tada, A., 1995. Applicability of numerical models to nonlinear dispersive waves. Coastal Engineering 24 (3-4), 297-313.

Pauw, W.H., Huijsmans, R.H.M., Voogt, A., 2007. Advances in the Hydrodynamics of Side-by-Side Moored Vessels, Proceedings of the 26th International Conference on Offshore Mechanics and Arctic Engineering, San Diego, California, USA. Paper No. OMAE2007-29374.

Saitoh, T., Miao, G., Ishida, H., 2006. Theoretical analysis on appearance condition of fluid resonance in a narrow gap between two modules of very large floating structure, Proceedings of the 3rd Asia-Pacific Workshop on Marine Hydrodynamics, Shanghai, China, pp. 170-175.

Suh, K.D., Lee, C., Park, W.S., 1997. Time-dependent equations for wave propagation on rapidly varying topography. Coastal Engineering 32 (2-3), 91-117.

Sun, L., Taylor, R.E., Taylor, P.H., 2010. First- and second-order analysis of resonant waves between adjacent barges. Journal of Fluids and Structures 26 (6), 954-978.

Tan, L., Lu, L., Liu, Y., Sabodash, O.A., Teng, B., 2014. Dissipative Effects of Resonant Waves in Confined Space Formed by Floating Box in Front of Vertical Wall, Proceedings of the Eleventh ISOPE Pacific/Asia Offshore Mechanics Symposium, Shanghai, China. Paper No. ISOPE-P-14-080.

Wang, G., Zheng, J.-H., Maa, J.P.-Y., Zhang, J.-S., Tao, A.-F., 2013. Numerical experiments on transverse

oscillations induced by normal-incident waves in a rectangular harbor of constant slope. Ocean Engineering 57, 1-10.

Wang, G., Zheng, J., Liang, Q., Zheng, Y., 2014. Analytical solutions for oscillations in a harbor with a hyperbolic-cosine squared bottom. Ocean Engineering 83, 16-23.

Xu, X., Yang, J.-M., Li, X., Xu, L., 2014. Hydrodynamic performance study of two side-by-side barges. Ships and Offshore Structures 9 (5), 475-488.

Yao, Y., Huang, Z., Monismith, S.G., Lo, E.Y.M., 2012. 1DH Boussinesq modeling of wave transformation over fringing reefs. Ocean Engineering 47, 30-42.

Zhao, D., Hu, Z., Zhou, K., Chen, G., Chen, X., Feng, X., 2018a. Coupled analysis of integrated dynamic responses of side-by-side offloading FLNG system. Ocean Engineering 168, 60-82.

Zhao, W., Milne, I.A., Efthymiou, M., Wolgamot, H.A., Draper, S., Taylor, P.H., Taylor, R.E., 2018b. Current practice and research directions in hydrodynamics for FLNG-side-by-side offloading. Ocean Engineering 158, 99-110.

Zhao, W., Wolgamot, H.A., Taylor, P.H., Taylor, R.E., 2017. Gap resonance and higher harmonics driven by focused transient wave groups. Journal of Fluid Mechanics 812, 905-939.

Zhu, D.-t., Wang, X.-g., Liu, Q.-j., 2017. Conditions and phase shift of fluid resonance in narrow gaps of bottom mounted caissons. China Ocean Engineering 31 (6), 724-735.

Zhu, H., Zhu, R., Miao, G., 2008. A time domain investigation on the hydrodynamic resonance phenomena of 3-D multiple floating structures. Journal of Hydrodynamics, Ser. B 20 (5), 611-616.